Microstructure evolution and infrared thermography applied to tensile failure of a dilatant polymeric foam

K. B. Bhagavathula[1*], J. S. Parcon[1], A. Azar[1], S. Ouellet[2], S. Satapathy[3], C. R. Dennison[1] and J. D. Hogan[1*]

[1]Department of Mechanical Engineering, the University of Alberta, Edmonton, AB T6G 2R3, Canada.

[2]Valcartier Research Centre, Defence Research and Development Canada, Quebec, QC, G3J1X5, Canada.

[3]Soldier Protection Sciences Branch, U.S. Army Research Laboratory, Aberdeen Proving Ground, MD 21005, USA.

Abstract

In this work, the authors study the thermo-mechanical tensile response of a dilatant polymeric foam, focusing on developing characterization and testing methodologies needed to better understand the links between temperature, microstructure and mechanical response in these materials. The authors study these links for a commercially-available shear-thickening foam, named D3O LITE D. Samples were tested in tension under quasi-static conditions for a strain rate of $0.1s^{-1}$ using an MTS 810 testing apparatus. Micro X-ray computed tomography (XCT) was used to study the evolution of microstructure (pore size and wall thickness) as a function of strain and this was achieved by developing MATLAB-based programs to probe pore sizes and wall thicknesses. The foam specimens were loaded until failure and this allowed to examine a variety of stress regimes, including elastic regime, inelastic regime, and failure. These mechanisms are observed in-situ using an infrared thermal camera which record temperature profiles and these are linked back to stress-strain, and temperature-strain responses of the material to understand them in better detail. For this material, the yield stress and elastic modulus were found to be 0.57±0.1MPa and 5.47±0.1MPa respectively, at a yield strain of 10±4%. At the time of failure, the

average temperature of the specimen was found to increase by ∼3∘ C and a local temperature increase of ∼8∘ C was observed in the failure region. These results represent some of the first tensile studies on shear-thickening foams in the literature, and the testing methodologies developed in this study will serve as the foundation for additional experimental and computational studies across a broader range of foam materials.

Keywords - Thermo-mechanical behavior, Shear thickening foam, Dilatant foam, Computed tomography, Infrared imaging, Microstructure

1. Introduction

Polymeric foams are widely used in many automotive [1, 2], aerospace [1–3], military [3, 4], and packaging applications [4]. Their energy absorbing capabilities and low density make them an ideal candidate for protection materials, such as personal protection equipment (PPE) like knee pads [5], and specific to this study, helmet liner materials [5, 6]. One specific type of foams are dilatant or shear-thickening polymeric foams which react like a rigid materials when subjected to high stress or deformation rates [7–9], making them considerable for protection materials. In the past few years, Traumatic Brain Injury (TBI) has received increased attention in all fields, especially the military. The main function of the inner liner of the helmet, generally made of closed cell polymeric foams [6], is to absorb part of the impact/ballistic energy and to reduce the amount of load transmitted to the head, which directly contributes to TBI. To make efforts toward improving typical foams used in helmet liners, there exist a number of studies on compressive [5, 10, 11], tensile [11, 12], shear [12], and fracture [13] behavior of these polymeric foams. In this present paper, we seek to understand the deformation mechanisms in tension for a recent shear thickening foam.

To fully exploit the energy absorbing capabilities of foam materials, it is necessary to understand, analyze, model, and validate the constitutive response of foams under multiple stress states. In the literature, limited attention has been given to tension and other stress states [11 – 13] and more attention to compressive states [1–3, 5, 10–12, 14 – 18]. Ayyagari et al.[15] and others[11, 13, 19, 20] note the necessity of studying and understanding the mechanical behavior in polymeric foams under complex stress states and recognize the importance of studying the behavior in various stress states which necessitates modeling of yield behavior in foams. These models are then used to determine parameters such as elastic moduli [11, 13], elastic collapse stresses [11], and failure strengths and strains [13] based on information from experiments, and microstructure, which enables industry to design better foam materials. Generally, polymeric foams have a definite isotropic compressive yield stress whereas dilatant foams tend to have a range of compressive yield stress at elastic-collapse [7, 11, 18, 21, 22]. In one study, Ayyagari et al. [15] define the entire yield surface of a material which need only two yield strengths parameters from uniaxial compression and uniaxial tension. In a separate study, Walter et al. [11] show in their model that the elastic moduli and failure strengths of polymeric foams increase linearly with foam density. Their phenomenological model predicts the entire constitutive response in both tension and compression. Ultimately, the benefit of creating models is gaining insights into how to control microstructure or composition (manufacturing methods) to improve the foam performance for specific applications. These models require mechanical parameters that are obtained from experimental data, and we seek to contribute data for future modeling purposes.

In many studies, authors point to the importance of microstructure (usually in terms of density [5, 10, 23] and cell sizes [5, 10, 24]) and failure (usually through a post-test microscopic assessment of the sample [10]) on the material response of polymeric foams. It is well recognized that

mechanical properties of polymeric foam materials depend on the properties of the base polymer material [4, 14], relative density [12, 20] (ratio of the foam density to the density of base material) and microstructural geometry (e.g., pore size and wall thickness) [5, 10, 24]. For example, Chen et al.[24] show the effect of variation of cell size and wall thickness on elastic and shear moduli of foams. In their study, material properties are estimated through experiments, cell size and thickness distributions of the foam are measured from Scanning electron Microscopy (SEM) images, and existing models are applied to predict stiffness of the foam. Chen et al. [24] also note that variability in the cell wall thickness and cell size is important in overall tensile and shear response; this is important to note for our study. In another study, Bouix et al. [5] show the differences in elastic collapse stress levels and plateau stress moduli that manifest due to microstructure differences in polypropylene foams. Also, the structural response of foams is strongly influenced by the cell geometry (foam apparent density, cell topology and anisotropy ratio) and by properties of the base material [23]. Thus, understanding the links between microstructure and mechanical properties is of great importance for designing next-generation foams.

Micro X-ray computed tomography (XCT) is a widely recognized characterization technique used to investigate the microstructure of a range of materials [3, 25–27]. With the development of XCT techniques, finite element models based on the reconstruction of real foams using CT techniques have also been reported by many studies [21, 28–30]. For example, Fahlbusch et al. [30] describe a Representative Volume Element (RVE) - based model that predicts failure behavior of closed-cell polymeric foams whose microstructure information is extracted through XCT. This model shows the numerical and experimental failure points in foams in 11 different stress states for which experimental data exist. In another study, Youssef et al. [21] study the local deformation mechanisms of a polyurethane foam in compression by means of XCT. In their study, the

tomographic data is used to reconstruct the microstructure of the foam, and by using the constitutive equations of the bulk material and finite element modeling (FEM) methods, the macroscopic response of the material is captured. There are other techniques to investigate microstructure such as Scanning electron microscopy (SEM) [6, 13, 31], Fluorescence microscopy [32], etc. but these are inherently two-dimensional and do not provide sufficient 3D information in a timely manor. In contrast, XCT offers an ability to determine 3D volumetric data in relatively short time (5-10 minutes), thus allowing researchers a tool to assess features at the microstructural level in 3D. Altogether, the literature demonstrates the importance of microstructure on the mechanical response of foams, and we seek to contribute to this understanding in this paper.

In addition to efforts made to investigate failure [13, 33], develop models [11, 15], and characterize materials [17, 34], the sensitivity of mechanical response to temperature in foams is also well documented [23, 35–37]. For two different foam materials, Williams et al. [36] show that shear strength and stiffness properties of the foams exhibit an inverse relation with temperature, whereas the shear strain at failure exhibits a linear relationship. Infrared (IR) thermography is one of the established methods to study the effects of temperature on failure and material behavior [38, 39]. Chrysochoos [38] demonstrate the effective use IR techniques to study material behavior such as thermo-mechanical characteristic analysis of fatigue mechanisms in polymers and steels. In a different study, Ohbuchi et al. [39] use thermal image analysis to visualize plastic deformation/crack propagation in stainless steel in quasistatic tension. This was developed by combining thermal image processing with Elasto-plastic finite element analysis coupled with transient heat conduction calculations. These studies demonstrate the importance of thermal studies on mechanical behavior of materials. In the present study, tensile tests are performed on a

dilatant polymeric foam and the distribution of the specimen surface temperature is measured by using infrared thermography techniques.

This current paper builds on past works investigating the effects of stress states, temperature, microstructure and failure on mechanical response of polymeric foams. The present study is an extension of the work performed in a study by Bhagavathula et al.[7], where only the rate-dependent compressive response was examined. In this current paper, we focus on understanding the evolution of pore size, spatial distribution and wall thickness on the behavior of this shear-thickening foam in quasistatic tension. As limited work is available in published literature on shear thickening foam materials, this study intends to establish an understanding of microstructural length scales in quasistatic behavior of our foams, accomplished through experimentation and characterization. This paper is comprised of the following sections: first, thermography techniques and sample preparation methods are established and described. Second, experimental methods are presented that include microstructure characterization techniques and mechanical testing methods, followed by the presentation of the experimental results. These results are supported by stress-strain curves, cumulative distribution functions of microstructural parameters, X-Ray tomograms, and infrared video images obtained from high-speed infrared camera. Finally, implications and contributions of this work are highlighted, and future directions are suggested.

2. Experimental Methods

In this study, a shear thickening foam obtained from D3O is studied. D3O foam is used in padding on sports equipment and currently investigated for use in ballistic protective equipment [40, 41]. The variant under investigation is D3O LITE D, which is a partially open and closed-cell polymer-based material. The foam density is reported as 0.22g/cc and the chemical composition is held proprietary by the manufacturer. Some of the physical and mechanical properties provided by the

manufacturer are listed on the manufacturer website [42]. The motivation in characterizing this material stems from the lack of testing of this highly marketed non-Newtonian shear-thickening material, and we want to determine the behavior of this material over various stress states and strain rates [7].

2.1. Sample Preparation for Mechanical Testing

Tensile dog bone specimens were used in this study and these were manufactured using water jet cutting, which is an accepted sample preparation technique in experimental studies [43]. The dimensions of the gage section were 20 mm in length and 10 mm in width with a thickness of 4 mm, which is governed by the thickness of the as-received foam sheet. The tensile dog-bone samples were designed with ASTM D3575 Standard [44] as a starting point (geometric ratios of the samples follow the standard), but were scaled down to allow for sufficient longitudinal displacement in the testing apparatus to load until failure. To aid in performing the infrared measurements, one of all the specimens' faces were completely painted black using an air brush. This is consistent with other practices in the literature [37, 39]. Care was taken to ensure that the samples end surfaces were parallel, and that minimum damage is induced to the edges during sample preparation. The sensitivity of material strengths to geometry and specimen-size effects are widely discussed in literature [13, 16], and we expect them to show similar differences in our strengths and those provided by the manufacturer as different testing conditions may have been followed. We note that potential differences in composition, pore size and wall thicknesses may also occur as a result of different sizes of received sheets.

2.2. Quasistatic tension experiments

The specimens were tested in tension at a quasistatic strain rate of $0.1s^{-1}$ using a Material Test System (MTS) - 810 machine. This assembly included infrared visualization capabilities with an

infrared high-speed camera - FLIR X6901sc, which enabled us to observe temperature changes observed during testing. Details of the camera are discussed in the next sub-section. Both camera and MTS were triggered manually at the same time, and synchronization was verified through comparison between when the piston displacement was first observed in the thermal images with the displacement data recorded by the MTS machine (no adjustments were necessary). To perform the tension experiments, the specimens were mounted on screw-type tension grips with adequate surface area provided for thermal conduction within the sample. A 10 kN load cell with a background noise corresponding to approximately ±1N recorded the time histories of the forces, and the displacement of the piston was measured to an accuracy of 0.001mm using linear variable differential transformer (LVDT) displacement sensor. The tension grips were connected to the load cell and the actuator displacement rate was set to be 2mm/s corresponding to a strain rate of $0.1s^{-1}$ in the sample. Specimens were driven to failure in all experiments. The engineering stresses are calculated by dividing the applied load by the original specimen gage surface area. The engineering strains are computed by dividing the gage displacement in the camera images by the original gage length.

2.3. Infrared Thermography methods

An infrared high-speed camera - FLIR X6901sc system was used in this study for temperature measurements. The infrared thermal images and temperature data were recorded at a rate of 100 frames per second. At this frame rate, the FLIR X6901sc system provided 640×512 pixel resolution was sufficient to capture the whole event until failure. The integration time was 1.0432 ms. For the camera temperature calibration, the FLIR X6901sc camera is placed within a temperature controlled chamber and set to visualize a blackbody outside the chamber through a hole in the chamber wall [45]. The chamber temperature is then cycled from ambient to highest

specified operating temperature, then down to lowest, then back to ambient. A correction curve is generated from the data recorded and saved in the camera as part of the factory calibrations. These measurements are compared to a National Institute of Standards and Technology(NIST)-calibrated thermocouple. The calibration is performed for a range of temperatures. The infrared camera directly records all data to an onboard Solid state disk (SSD). To obtain temperature measurements during experiments, the detector output of the thermal camera is estimated from emissions of both target body and that of background. These emissions depend on ambient temperature, T_a (∘ C), target temperature, T(∘ C),and target emissivity ϵ. The measurement principle applied in this thermography method is given by:

$$V(T, T_a) = \epsilon W(T) + (1 - \epsilon) W(T_a) \tag{1}$$

where V(T,T_a) is the detector output, W(T) is the Black body emission energy, ϵW(T) is the emission of the target, and (1-ϵ)W(T_a) is the background emission. The emissivity of the target body depends on its surface condition. The accuracy of temperature measurement increases with increase in the emissivity of the surface [37, 39]. For example, for highly reflective (polished) surfaces, the emissivity and corresponding temperature readings will be lower. This has been a challenge for ductile materials [37], and has resulted in many authors painting their surfaces black [37, 39]. In this study, following convention, the target specimen was sprayed with black paint to obtain a higher emissivity of 0.92. The accurate measurement techniques of emissivity have been proposed [46], but there are many difficulties because of various kinds of errors, especially the atmospheric transmission coefficient. The coefficient of the band transmittance of the atmosphere should be estimated accurately because it is an important factor for measuring temperature with such a method when the distance between the measured surface and the camera is very large [46]. In our experiments, the distance between the camera and the object was only 0.25 m, so it can be

assumed to be unity in this experiment. In the experiment, the ambient temperature and atmosphere temperature was recorded to be 21 ∘C. Before the experiment, the specimens were kept in the test room for a long time to equilibrate to the room temperature.

The temperature data measurement was tried using the FLIR ResearchIR software's rectangular ROI function and conforming to camera positioning, selecting a fixed ROI on the sample surface for the entire course of the experiment was not possible, necessitating an external program for temperature data analysis. This software allowed for export of csv files containing individual pixel temperatures of every infrared image. These csv files were imported to MATLAB and a program was designed track displacements and to calculate average temperature on the sample. The infrared images are also exported as monochromatic tiffs and the edge of the tension grip is tracked using image processing techniques. The infrared image index is converted to strain by synchronizing with the MTS data, and monochromatic TIFFs and csv files are synchronized through strain. The temperature data corresponding to those pixels containing the grips are deleted. The background pixels are also deleted using a threshold background temperature.

2.4. X-Ray Computed Microtomography

Synchrotron radiation based X-ray microtomography was used at the Biomedical Imaging and Therapy (BMIT) facility - Canadian Light Source (CLS)[47] 05ID-2 - SOE-1 hutch, Saskatoon, to obtain volumetric information of the microstructure. The facility's capabilities are mentioned in table 1 [48]. Samples of 5 mm × 5 mm × 4 mm were manually cut from the center of the sample gage section for imaging. This was done so as to accommodate the sample on the mounting pad. The samples were mounted with their loading axis parallel to the scan direction. The beam energy was set to 30 keV. The imaging setup used a Hamamatsu ORCA FLASH 4.0 detector. This detector provided an effective voxel resolution of 3 μm where the distance between the specimen

and detector was 20±1 mm. This resolution provides sufficient scan volume in order to sufficiently resolve the cell wall thickness (3 to 30 μm), and pore size (30 to 120 μm) analysis. The sample loading stage operated in intermittent motion and each sample scan comprised of 900 tomograms being acquired within 10 minutes over 180∘ of rotation. Reference images without the sample, and dark images without X-rays were also obtained before and after every scan to increase the quality of images during background filtering reconstruction.

Table 1: Beamline parameters of 05ID−2 − SOE−1

Source	Superconducting (SC) Wiggler
Energy Range	25 − 150 keV
Wavelength	0.5 − 0.08 Angstroms
Resolution $\Delta E/E@E$	M_1 CT:10^{-3} andM_4 KES:10^{-3}
Beamline Length	55 m
Maximum Beam Size (Horizontal x Vertical)	220 mm × 11 mm @ 55 m
Maximum sample-detector-distance	6 m

Three-dimensional reconstruction of the tomograms was achieved using a MATLAB- based reconstruction program. This program performs 2D characterization on slices obtained from the 3D scans of the sample volume. To demonstrate these capabilities, we show a flow chart of the image processing methodology adopted in this study in Figure 1. Figure 2 shows a sample tomogram and sub-sequential image processing applied to it and is used to explain the flow chart

in Figure 1. First, a threshold ranging from 0 to 1 is defined for converting greyscale images to binary images. The images are converted to data type uint16 for better handling and processing, and to minimize loss of quality. The tomograms have varying contrast and brightness at different slices of the foam. The brightness is adjusted and the contrast is sharpened to obtain images with consistent lighting exposure to improve segmentation of distinct pores and walls. For example, the intensity of each pixel in greyscale images varies from 0 to 65535 corresponding to black and white pixel, respectively, for data type 'uint16'. Depending on the amount of contrast in the original image, the threshold is varied manually to obtain the best result. For the tomograms obtained from CLS, it was kept at a constant value of 0.34. Using the threshold, the adjusted and converted image is converted to binary values. Binarizing often results in several noises and aliases being created. Most of these unwanted features stand out because they are often small and large in terms of pixel area. They are filtered out by defining a range of pixel sizes to delete. In the binarized images, walls have a value of 0, and the pores have a value of 1, and this is shown in Figure 2(b). Each slice is read and stored in a large 3D array for processing. Following this, a series of image processing operations are performed to segment the pores.

After image processing, the binarized image is stored in a 3D array. The segmented image is then visualized by plotting it and it is determined whether or not the image segmentation is acceptable. Parameters in the image processing step are varied until a desirable segmentation is obtained. Using the binarized 3D image, a disk structuring element is used to grow the pore size on the image in order to thicken the walls using a function called 'erosion'. The disk size was appropriately selected depending on the sizes of the pores for image erosion. Erosion is then implemented to close walls that may have been opened and filtered out during the image processing step. This process further minimizes the noise for improved data analysis. Similar to the output binarized

image, the eroded image is visualized to determine if the erosion is appropriate as shown in Figure 2(c). After eroding the walls, the pores that are along the border of the scan are closed and filtered out. These regions are not of interest for data analysis since they are incomplete. The image without the border pores are stored in another variable. The eroded image without border pores are used to determine the pore sizes and wall thicknesses.

Using the output binarized images, the connectivity of pores in 3D is used to find the connected regions in the images, and the coordinates of the 3D pore centroids are calculated. The coordinates of the pore centroids and resolution of the scan are input into a custom function that calculates the pore diameters and wall thicknesses. In this custom function, the pore diameters and wall thicknesses are calculated by counting the number of white and black pixels, respectively, in 6 orthogonal directions. The coordinates of the centroids are used as the starting point for all the pores. Corresponding to each centroid, 3 diameters (1 diameter in each x,y and z directions) and 6 wall thicknesses are calculated. These values are stored in a 3-D array for further data processing and plotting. For porosity measurements, the pore volume was calculated using the reconstructed XCT scans and was subtracted from the total sample volume.

3. Experimental Results

Three trials for tension were performed at the same nominal strain rate to verify repeatability of the material behavior. We show the stress-temperature-strain curves in Figure 3. The x, y_1 and y_2 axis represent strain (%), stress (MPa) and temperature change ($^{\circ}$C), respectively, in a linear scale. The solid black curve (trial 1) is highlighted for clarity as we later use the figure to discuss temperature curves and microstructure changes, presented in a subsequent section. The dotted curves for trials 2 and 3 are shown for repeatability. In the quasistatic tension experiments, the yield stress was measured to be 0.57±0.2MPa corresponding to a yield strain of 10±4% across all

samples. The elastic modulus in the corresponding strain range was measured to be 5.47±0.1MPa. In the inelastic deformation regime, the stress was found to linearly increase with strain at rate of 0.44±0.05MPa ϵ^{-1}. The inelastic deformation regime extends until a strain of 298±7% is achieved, and no other notable features are observed on the stress-strain curve until failure. The failure strength and strain was measured to be 1.99±0.05MPa and 305±5% across all samples, respectively. To observe the effects of black paint on the tensile response, one experiment was performed under similar experimental conditions with an unpainted specimen. This trial is represented by trial 3 (T3) in Figure 3 with a solid blue curve. As observed from the figure, there is no effect of presence of black paint on the mechanical response.

3.1. Infrared Thermography results

Shown in Figure 3 are the stress-temperature-strain curves of tensile response of D3O LITE D. As noted earlier, the y_2 axis represents temperature changes observed on the specimen surface. To account for effects of atmospheric conditions, absolute temperature differences (ΔT) observed on the specimen surface are reported here (note the y-axis on the right side of the graph in Figure 3). The black dotted curve represents the temperature changes observed using a local ROI at the failure region. As observed from the curve, the temperature initially decreases by ~0.05∘ C from 0% strain until a strain of ~25% is reached in the sample. Following this, the temperature continues to increase steadily at a rate of 1.02±0.05∘ Cϵ^{-1} in the whole sample until failure. This drop and rise in temperature corresponds to the presence of an inflection on the curve at ~30% in the stress-strain curve corresponding to the offset of the elastic regime. At a strain of ~300% at the region of failure, the temperature starts to increase rapidly at a rate of 90±5∘ Cϵ^{-1} as the specimen starts to fail. A peak temperature rise of approximately 8∘ C is observed at the region of failure. The dashed black curve represents the average specimen temperature changes observed using a large

ROI over the specimen cross section. A similar inflection is observed on the average specimen temperature curves as well, suggesting that the initial thermal response is globally similar throughout the sample. This can be corroborated from the figure where dashed and dotted black curves overlap each other until a strain of 30% is reached in the specimen. Hereafter, the average temperature of the specimen continues to rise steadily at a rate of $1.02 \pm 0.05 \circ C\epsilon^{-1}$ until failure. No notable features are observed on the temperature-strain curve until failure.

Next, we consider global measurements on the surface of a specimen by examining individual images from the infrared camera. Figure 4 shows the infrared video frames from one of the quasistatic tension experiment obtained using the FLIR X6901sc infrared camera at a framerate of 100Hz. Conforming to positioning of the camera, and using a fixed ROI for entire course of the event, a small ROI was selected as visualized in Figure 4. The dashed black curve in the temperature-strain axes in Figure 3 represents the average specimen temperature changes observed using the selected ROI over the specimen gage section. The temperature then continues to rise at a rate of $1.02 \pm 0.05 \circ C\epsilon^{-1}$ until a strain of 300% is reached in the specimen. We then observe some large temperature fluctuations on the curve at higher strains but no further rise in overall temperature. This is caused due to the positioning of the ROI. At strains <150%, an appreciable amount of surface area of the entire gage section is under observation but as strain increases, a large considerable area remains outside the fixed ROI. At strains higher than <150%, the specimen elongates in such a way that the gripped area of the dog bone specimen starts to appear inside the selected ROI. This presence reduces the measured rate of temperature increase as the gripped area does not contribute to the thermal measurements. This effect increases with increasing strain, and at strains higher than 225%, the measured temperature plateaus until failure. It is to be noted that small changes in emissivity and surface condition occur during tensile testing and the errors caused

by these effects are infinitesimally minute when compared to the overall temperature rise. The uncertainties associated with the ROI selection and corresponding temperature measurements were found to be less than 1%. This was found from temperature measurements using different size and shape ROIs on multiple locations on the sample surface. Overall, the infrared camera provided consistent results and this paper demonstrates that heat release associated with tensile testing can be successfully monitored using high-speed infrared imaging.

3.2. Microstructure results

Shown in Figure 5 is a composite figure of XCT images showing evolution of microstructure in quasistatic tension. Note the loading direction is in the y direction. These images are obtained through XCT slices of the samples' center starting from 10% strain, at increments of 20% strain until 100% strain. Image (1) shows the scan orientation of the specimens, where it can be observed from image (1) that there are irregularly shaped pores with a circularity of ~80% [7]. Some form of additives appear to be concentrated at the pore boundaries which are visualized by small white dots in the XCT images. Images (2) to (6) shows the differences in microstructure observed with increase in strain. There are no signs of permanent damage or pore elongation observed in image (2) as the pores remain intact. Signs of damage to the cell walls are observed in image (3) and they become increasingly prominent in images (4) to (6). Pore elongation and cell wall stretching also becomes more visually apparent in images (4) to (6). As observed from the images, the foam has a stochastic pore structure. The quantitative measurements of pore sizes and wall thickness as a function of strain are explored next.

3.2.1. Pore characterization: shapes and sizes

The procedure for determining the pore size and wall thickness measurements were discussed earlier. Note, we recognize that foam samples recover up to ~20% of the applied strain following

tension testing, however, as will be shown, insights can be gained as to what pore size length scales are activated during testing. Pores with sizes less than 250μm were considered for pore size measurements based on visual confirmation from XCT scans. Now that interesting characteristics of the pore size measurements have been identified, the effect of tensile loading on pore sizes is examined next. Here, we plot the cumulative distribution of pore size in both x and y directions. The cumulative distribution is defined as:

$$G(x) = \int_0^x g(\bar{x})d\bar{x} \tag{2}$$

where $g(\bar{x})$ is the probability distribution of pore sizes. The pore size data set is a discrete set of n pores with sizes of l_i (i=1...n). Ordering this data for increasing pore size, and assigning a probability of 1/n to each pore, the normalized empirical cumulative distribution function, or eCDF, can be computed as the sum of these probabilities:

$$G_e(\ell) = \frac{1}{n}\sum_{i=1}^{n} I(\ell_i \leq \ell) \tag{3}$$

where the indicator function I has a value of 1 if $\ell_i \leq \ell$ and 0 otherwise. For each tomography scan, a total of ~70,000 pores were considered for size and thickness measurements. Shown in Figure 6 are the eCDFs which are used to identify the likely range of the pore sizes and trends. This is achieved by looking at the values between the 10th and 90th percentiles. This range is projected to be between $40\mu m$ and $120\mu m$ in both x and y directions for a pristine sample. In Figure 6, D_x and D_y represent the pore sizes in x and y directions respectively. With increasing strain up to 30%, a peculiar behavior is observed among the curves that smaller pores tend to elongate in both x and y directions while larger pores tend to contract in both directions. For strains greater than 30%, the pore size distribution follows a constant and an expected trend [12, 13] where all pore sizes reduce in the x direction and increase in the y(loading) direction with increasing strain. From Figure 6, when the specimen is loaded in tension at a initial strain range of

$0 - 70\%$, it is observed that pores sizes of D~$100\mu m$ show larger changes in the x direction when compared to y direction. This is caused due to smaller pores getting stretched initially, and thus increasing the number of pores that are greater than $100\mu m$. At strains greater than 70%, the differences in pore sizes with $D > 100\mu m$ becomes more prominent and this can be visualized by 90% and 100%strain curves having bigger pore diameters than other strains. For the 90% and 100% strain curves, there are more number of bigger pores possibly due to tearing and ripping of walls of small pores, resulting in coalescence into bigger pores.

3.2.2. Wall thickness characterization

Shown in Figure 7 are the eCDFs of the wall thicknesses for strains of 0% to 100%. Wall thickness sizes less than $50\mu m$ were considered based on visual confirmation from XCT images. In Figure 7, T_x and T_y represent the wall thicknesses in x and y directions respectively. The wall thickness range is projected to be between $3\mu m$ and $30\mu m$ in both x and y directions for a pristine sample and also profiles of T_x and T_y are similar. For all samples, it is consistent that $T_x < T_y$ as strain in the y-direction increases. These observations are made from looking at individual plots of each sample with T_x and T_y on the same plot. When compared across samples, both T_x and T_y decreases as strain increases. This trend is followed consistently throughout for T_x. For T_y, it generally follows a similar trend but with slight variations. T_y for a pristine sample is very different from the other strains for T_y. Also, there is another effect that makes T_y smaller as strain increases. This is possibly due to tearing of walls, making thicker walls thinner. Although relative differences between these values are small, these variations in wall thickness evolution are to be noted.

3.2.3. Percentile plots

To better understand the evolution of microstructure during the quasistatic tensile response of this D3O LITE D foam, all quantitative microstructure data is consolidated and presented in form of percentile plots for both pores sizes and wall thickness variations in Figure 8. The percentile plots are obtained from the CDF function for $G(x) = 0.1, 0.25, 0.5, 0.75$ and 0.9 (e.g. G(x)=0.1 for the tenth percentile). This is done to clarify trends observed in the cumulative distribution plots. In Figure 8(a), the x and y axes represent pore size (μm) and strain (%) respectively, and wall thickness (μm) and strain (%) respectively in Figure 8(b). A single color scheme is used for both pore size and wall thickness percentile curves, and are denoted by $x - P_i$ and $y - P_i$ in the common legend. The percentile plots are denoted by P_i where i represents the strain percentage. In both subplots, porosity is plotted as a function of strain which gives more basis of discussion. However, it is to be noted that porosity calculations were performed on the final segmented images from pore size measurements. Since different disk sizes were used to compute the segmented images for different strains, there is approximately 1% error in porosity calculations.

Shown in Figure 8(a) are the percentile plots corresponding to those in Figure 6. At strains less than 20%, the trend is clearly observed that smaller pores tend to deform first and they deform equally in both x and y directions. This results in a sudden decrease in porosity. As strain increases greater than 20%, it is observed that pores of all sizes show expected behavior that sizes increase in y direction and decrease in the x direction. This results in a near constant rate of increase in porosity of the material. From Figure 8(a), it is also observed that the number of pores with size < 100μm is smaller for higher strains than the pristine sample. This is consistent with the previous statement that as smaller pores gets stretched, there will be fewer of the small pores. Shown in

Figure 8(b) is the percentile plots for the wall thicknesses in both x and y directions. Again, we discuss percentiles of $G(x) = 0.1, 0.25, 0.5, 0.75$ and 0.9. From the figure, it is observed that there is no effect of tensile loading on evolution of wall thicknesses throughout the strain range. This implies that the stress response is primarily governed by geometry change of the pore structure. Generally, with increase in strain, the trend of the observed microstructural length scales tend to follow a very slight linearly increasing path until onset of failure occurs. And as noted before, bigger pores are susceptible for larger pore size variations and this true until the onset of localization is observed.

4. Discussion

This paper investigated the thermo-mechanical behavior and microstructure evolution during quasistatic tensile failure of a shear-thickening polymeric foam. It is important to have a better understanding of behavior of these materials since this class of foams are currently being employed in energy absorption equipment (e.g., helmet liners for US team sports such as Football, Baseball and Ice Hockey, as well as protective inserts for Motorcycle jackets) and also in some military applications [40, 41]. Limited data on these foams, and shear thickening foams in general, exist in the literature, and so this paper seeks to make contributions towards better understanding how microstructural features and thermal response of these types of foams may be related to quasistatic tensile failure. In what follows, the authors discuss the results of behavior of this foam in the context of their general understanding of how polymeric foams behave in tensile loading, highlighting our key results where necessary. The results obtained through infrared thermography and mechanical measurements, as well as qualitative and quantitative data obtained from Micro X-ray computed tomography provide the basis for this discussion. First, each regime in the

stress−strain curve in Figure 3 is discussed in greater detail with the help of microstructure data, temperature−strain curves, and infrared video images from Figure 4.

4.1. Elastic regime

The first part of the stress−strain curve is the elastic regime, which represents strains less than $10 \pm 4\%$ for D3O LITE D. For polymeric foams, the linear-elastic strain limit is found to be different for different foam materials throughout literature [11, 13]. Limited data exists on the thermal response of foams in the literature. For the D3O LITE D material studied here, we observe that the average temperature of the sample initially decreases by $\sim 0.05^{\circ}\mathrm{C}$ over $\sim 30\%$ strain, which corresponds to the end of elastic regime of the material. This decrease is believed to be a result of a small decrease in the emission surface area during tensile loading. In the infrared images, no notable features are visible on the specimen and temperature is uniformly distributed across the surface in the elastic regime. From the XCT data, it is visualized in images (1-2) of Figure 5 that larger pores remain the same sizes and there is no visible damage to the microstructure in the elastic regime ($< 10 \pm 4\%$). In this range of strain, it is observed from Figure 8(a) that all pore sizes do not undergo deformation, but there is a slight increase in the porosity. This is believed to be caused due to relative differences in sufficient permanent elongation/contraction being experienced by the different pore sizes as seen in Figure 6 and Figure 8.

4.2. Inelastic regime

Over the inelastic deformation regime, the stress in the sample rises linearly with strain at a rate of $0.44 \pm 0.05\mathrm{MPa}\epsilon^{-1}$ over 30 to $298 \pm 7\%$ range of strain. It is to be noted that elastomeric foams can undergo much higher strains than those experienced before the linear-elastic strain limit and the deformation can still be mostly recoverable, but is non-linear [16]. After a strain of $20 \pm 5\%$ is reached in the specimen, there is an inflection in the temperature curve at roughly the point

in the stress-strain curve that corresponds to post elastic part. The temperature starts to increase beyond a strain of $30 \pm 5\%$ resulting from thermal energy release in the process of micro−cracking of the cell walls. Over this entire range of strain, average temperature rise of 2 degrees is observed within the specimen at the end of the inelastic regime. The temperature initially decreases during the elastic part and then steadily increases. In XCT images (3-6) of Figure 5, it can be observed that with increasing strain in the y direction, pore sizes show visually observable differences in sizes. For strains greater than 30%, it can also be observed from the images that pore boundaries and walls show signs of damage and permanent deformation. The porosity is observed to linearly increase at a rate of $0.075\%\epsilon^{-1}$ until failure.

4.3. Pre-failure and Failure regime

The pre-failure regime starts at a strain of $298 \pm 7\%$ for D3O LITE D. The ultimate tensile strength was measured to be $1.99 \pm 0.05\text{MPa}$ which the observed during failure and the failure strain was measured to be $305 \pm 5\%$ across all samples. Prior to failure, minor fluctuations in temperature are observed and this is likely due to the result of localization because of pore tearing. At the begining of pre-failure regime, a local heat zone is observed in image 7 of Figure 4 which indicates local failure being initiated within the sample. In Figure 3, the dotted black curve shows the temperature measured across the region of failure. In the local failure region, there is sharp rise in temperature by $\sim 8^{\circ}\text{C}$ degrees observed at the point of failure at a strain of $305 \pm 5\%$. This heat spot results from energy release in the course of the breaking of chemical bonds during failure. At the onset of failure, the failure zone initiates at a point on the specimen perimeter and failure propagates at $\sim 0.05\text{m/s}$ through the sample leading to failure. XCT images and microstructure data corresponding to strains $> 100\%$ to failure are not shown or discussed as steady trends in both stress−strain, and temperature−strain curves are observed throughout, and no deviations are

observed until failure. The contributions for XCT of foam can provide insights into the cell-by-cell deformation of the foam, which is hypothesized by Di Landro et al. [6], Mills et al. [18] and other microstructure based models.

5. Conclusion

The thermo-mechanical quasistatic tensile response of a shear-thickening polymeric foam D3O LITE D is explored at a strain rate of $0.1\mathrm{s}^{-1}$. Important microstructural parameters like pores sizes ($40\mu\mathrm{m}$ to $120\mu\mathrm{m}$) and wall thicknesses ($3\mu\mathrm{m}$ to $30\mu\mathrm{m}$) have been identified using Micro XCT and image processing techniques. Overall, pore sizes were found to increase linearly with increasing strain, and it was observed that bigger pores ($\mathrm{D} > 100\mu\mathrm{m}$) are susceptible for larger variations in size when compared to smaller pores. The changes in wall thicknesses were comparatively negligible through the entire strain range (0 to $305 \pm 5\%$). The thermal response of this foam during quasistatic tensile testing was established using Infrared Thermography and the average specimen temperature was found to increase by $\sim 3°\mathrm{C}$ and concurrently a local temperature increase of $\sim 8°\mathrm{C}$ was observed at the failure region over a strain of $305 \pm 5\%$. These inferences are supported by stress-strain curves, XCT images of original and evolving microstructure, eCDFs of pore size and wall thicknesses, and high speed infrared thermography images. As this is the first time that the D3O LITE D foams have been characterized in this way, the authors believe these experimental results will also serve as a good starting point for impactful modeling [6, 18]. The results of the tests performed and the future tests will be put together to make models to predict the effect of microstructure, temperature and stress states on the mechanical response of shear thickening foams.

6. Acknowledgments

This research was sponsored by the Army Research Laboratory and was accomplished under Cooperative Agreement Number W911NF-16-2-0083. The views and conclusions contained in this document are those of the authors and should not be interpreted as representing the official policies, either expressed or implied, of the Army Research Laboratory or the U.S. Government. The U.S. Government is authorized to reproduce and distribute reprints for Government purposes notwithstanding any copyright notation herein. Research described in this paper was performed at the BMIT facility at the Canadian Light Source, which is supported by the Canada Foundation for Innovation, Natural Sciences and Engineering Research Council of Canada, the University of Saskatchewan, the Government of Saskatchewan, Western Economic Diversification Canada, the National Research Council Canada, and the Canadian Institutes of Health Research. We also greatly acknowledge the in-kind support of Defence Research and Development Canada. We also thank Bernie Faulkner of Department of Mechanical Engineering, University of Alberta for his help with experimental setup and Christopher S Meredith of Army Research Laboratory for his insightful discussions.

List of Figures

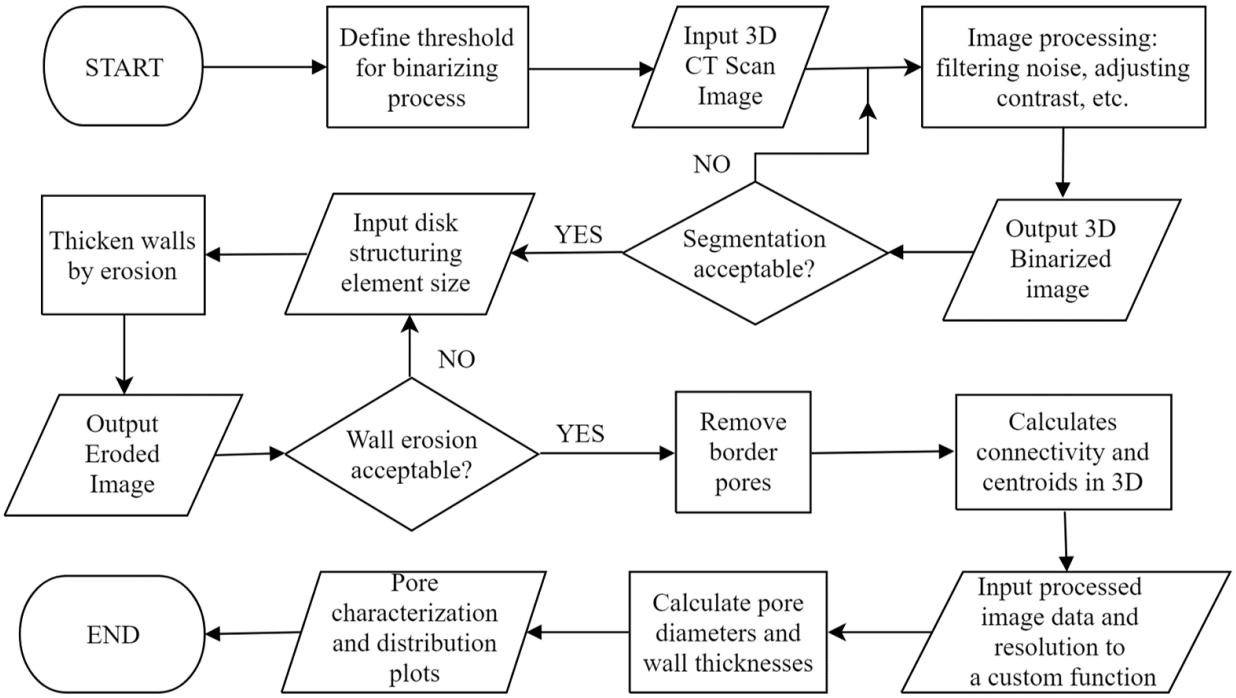

Fig. 1: Flow chart of the MATLAB program used to reconstruct and analyze the Micro X-ray computedtomography scans of the polymeric foam specimen obtained from Canadian Light Source.

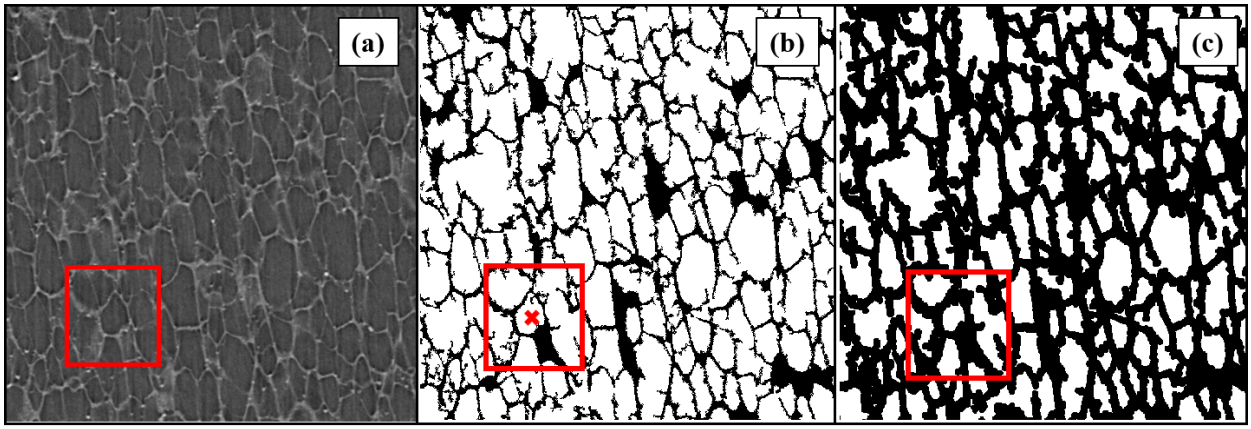

Fig. 2: Segmented XCT image used to identify locations of additives and throats (constrictions between two pores) within the sample, and for reconstruction. (a) Original XCT image with a specific pore in interest shown in the red box. (b) Binarized image after image segmentation with centroid. (c) Output erored image showing thickened walls for closing off pores that opened up during binarization which is used to calculate pore centroids.

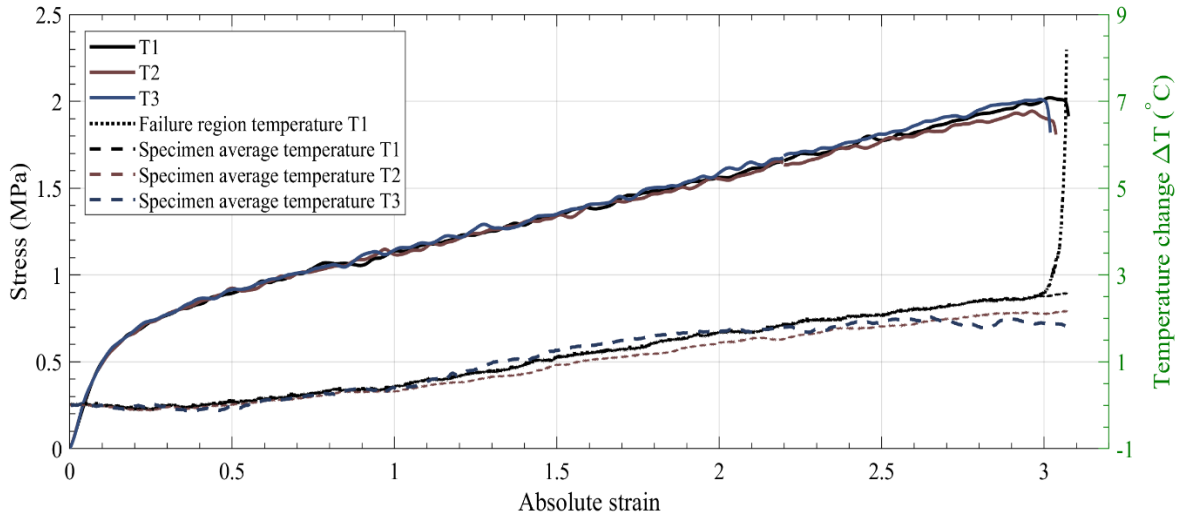

Fig. 3: Figure showing Stress-Temperature-Strain (y-y-x) graph where black curve represents quasistatic tensile response of D3O LITE D foam. The black dashed curve represents average temperature measured across the entire gage section tracked through time. The black dotted curve represents temperature measured across the cross-section at localized region of failure tracked through time. The temperature of the sample is observed to uniformly increase with respect to strain until failure is initiated where a localized temperature increase of ~ 8°C is observed.

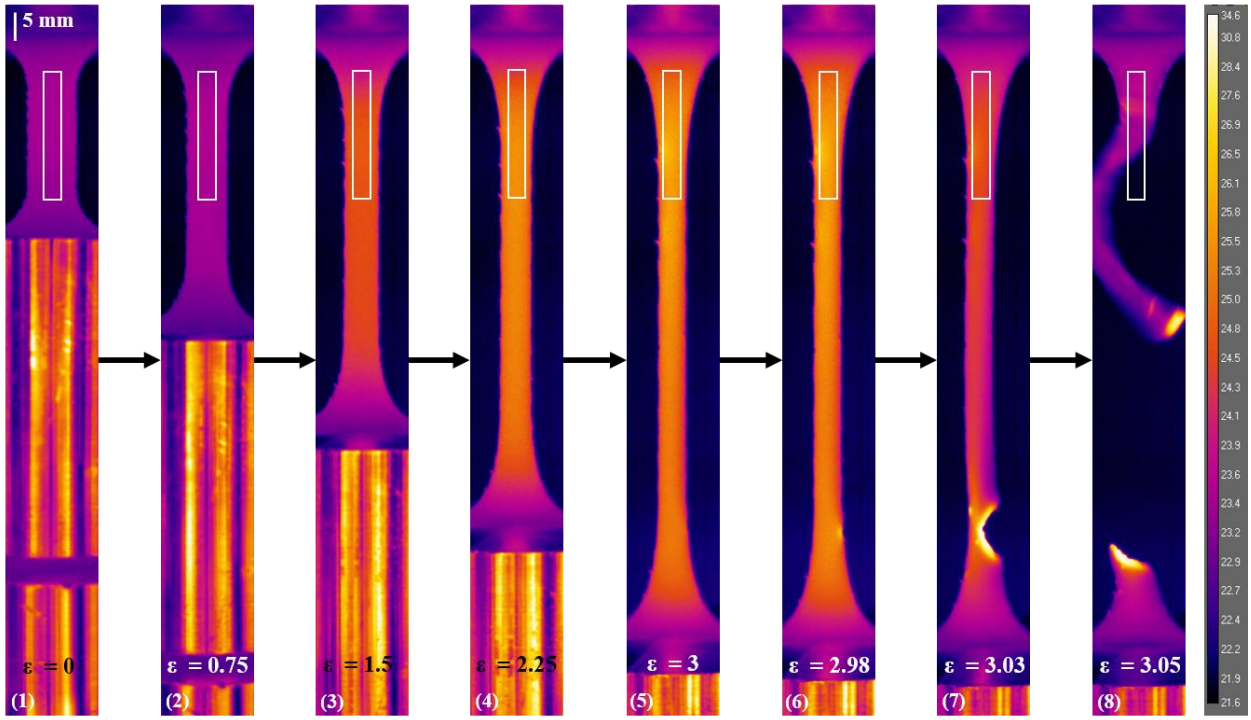

Fig. 4: Thermal camera video frames from the quasistatic tension experiment at a strain rate of $0.1s^{-1}$ obtained using FLIR X6901sc at 100Hz. Inter-frame strains and specimen lengths are denoted. Color bar on the right denotes temperature scale in Celsius. The last three images emphasize localized temperature increase that is observed at the failure region at a failure strain of 3.05.

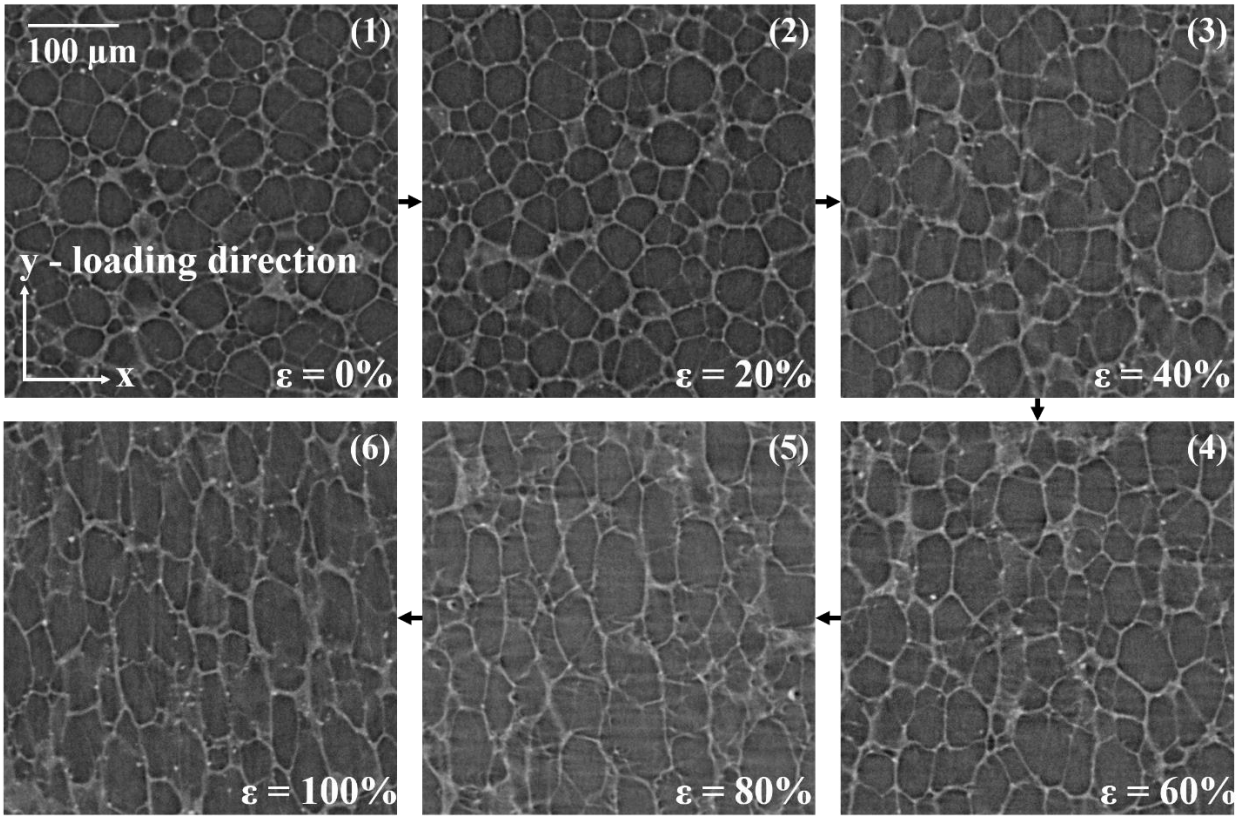

Fig. 5: Composite figure showing microstructure evolution in quasistatic tension through XCT images of the sample center at increments of 20% strain until 100% strain. Visibly distinguishable differences in pore sizes are observed from strains greater for 30%. Micro−cracking and damage of the cell walls is also observed for strains greater than 30%.

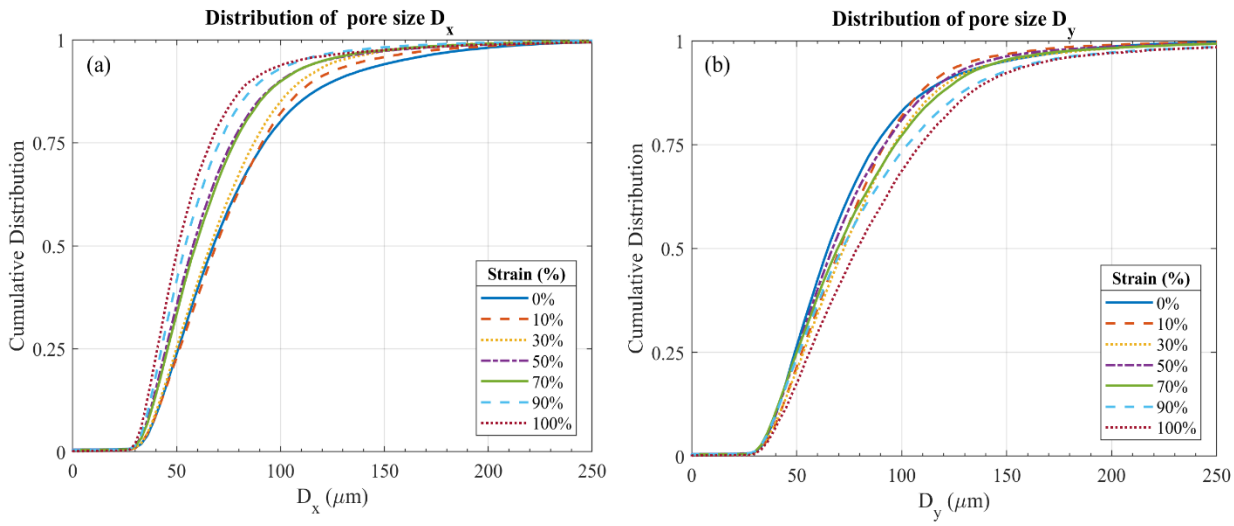

Fig. 6: Cumulative Distribution Function (CDF) plots of pore sizes shown for strain increments of 10% until 100% for quasistatic tension of D3O LITE D foam for both x and y directions.

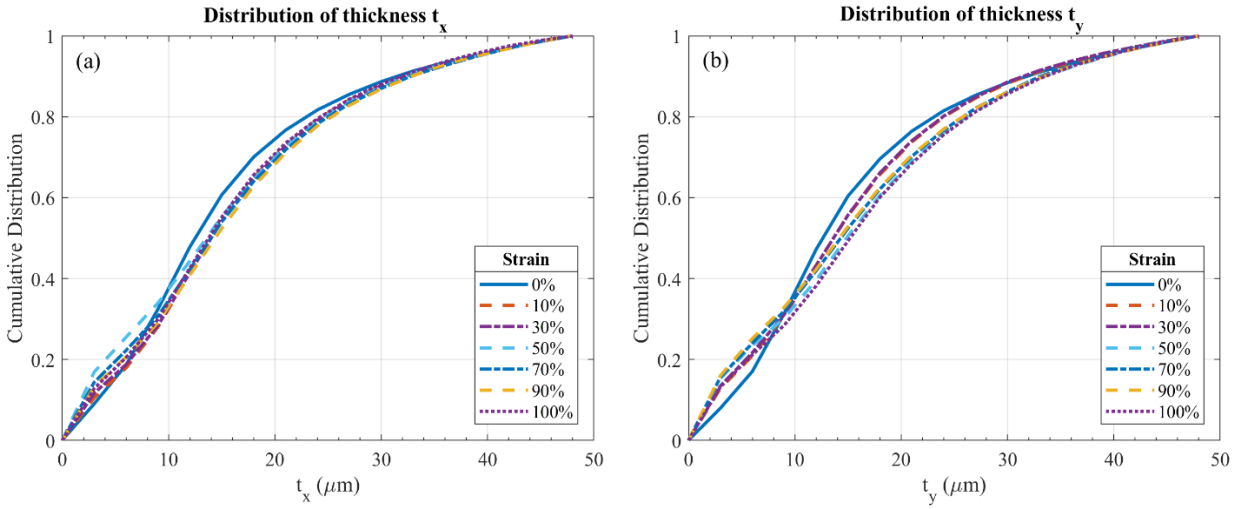

Fig. 7: Cumulative Distribution Function (CDF) plots of wall thickness shown for strain increments of 10% until 100% for quasistatic tension of D3O LITE D foam for both x and y directions.

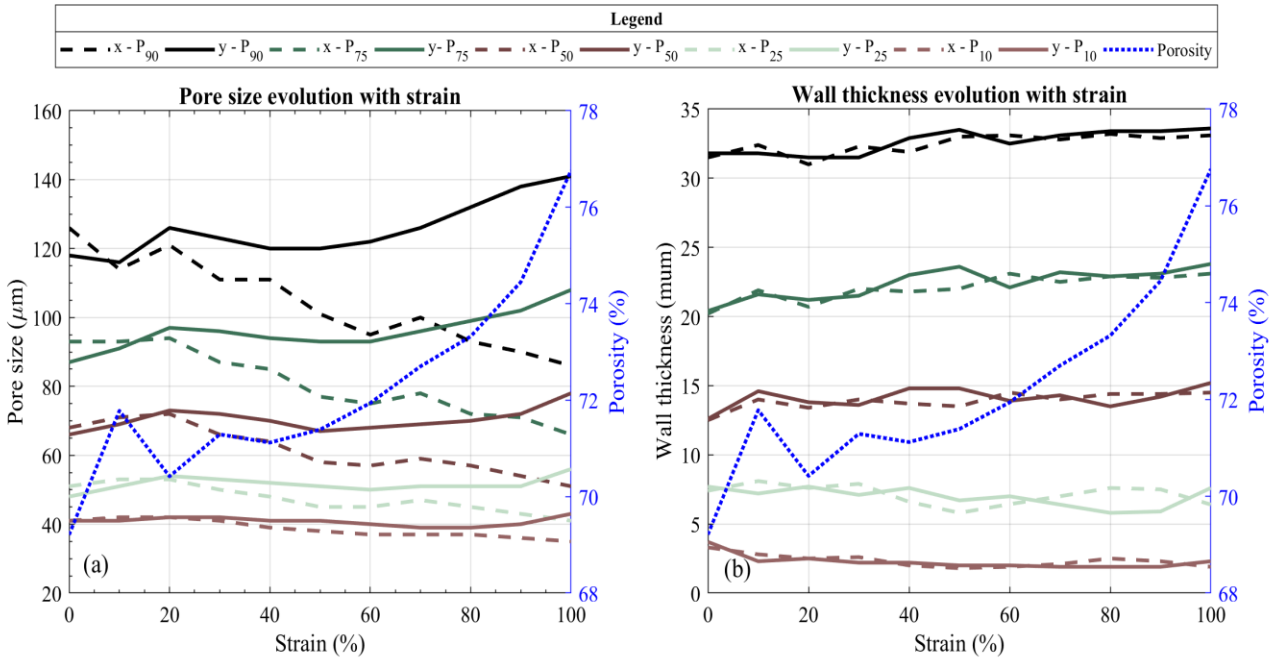

Fig. 8: Compiled percentile plots of pore size and wall thickness shown for 10th, 25th, 50th, 75th and 90th percentile in both directions for quasistatic tension of D3O LITE D foam. Plot also shows evolution of porosity with strain.

References

[1] G. Subhash, Q. Liu, and X. L. Gao, “Quasistatic and high strain rate uniaxial compressive response of polymeric structural foams,” International Journal of Impact Engineering, vol. 32, no. 7, pp. 1113–1126, jul 2006.

[2] W. Chen, F. Lu, and N. Winfree, “High-strain-rate compressive behavior of a 548 rigid polyurethane foam with various densities,” Experimental Mechanics, vol. 42, 549 no. 1, pp. 65–73, 2002.

[3] B. M. Patterson, N. L. Cordes, K. Henderson, J. J. Williams, T. Stannard, S. S. Singh, A. R. Ovejero, X. Xiao, M. Robinson, and N. Chawla, “In situ X-ray synchrotron tomographic imaging during the compression of hyper-elastic polymeric materials,” Journal of Materials Science, vol. 51, no. 1, pp. 171–187, 2015.

[4] A. Shukla, Blast Mitigation, A. Shukla, Y. D. S. Rajapakse, and M. E. Hynes, Eds. New York, NY: Springer New York, March 2014.

[5] R. Bouix, P. Viot, and J. L. Lataillade, “Polypropylene foam behaviour under dynamic loadings: Strain rate, density and microstructure effects,” International Journal of Impact Engineering, vol. 36, no. 2, pp. 329–342, 2009.

[6] L. Di Landro, G. Sala, and D. Olivieri, “Deformation mechanisms and energy absorption of polystyrene foams for protective helmets,” Polymer Testing, vol. 21, no. 2, pp. 217–228, jan 2002.

[7] Bhagavathula, K. B., Azar, A., Ouellet, S., Satapathy, S., Dennison, C. R., & Hogan, J. D. (2018). High Rate Compressive Behaviour of a Dilatant Polymeric Foam. Journal of Dynamic Behavior of Materials, 4(4), 573-585.

[8] S. Signetti, M. Nicotra, M. Colonna, and N. M. Pugno, “Modeling and simulation of the impact behavior of soft polymeric-foam-based back protectors for winter sports,” Journal of Science andMedicine in Sport, vol. 0, no. 0, nov 2018. [Online]. Available: https://linkinghub.elsevier.com/retrieve/pii/S144024401831065X

[9] J. Ding, P. J. Tracey, and P. G. Whitten, “Review on shear thickening fluids and applications,” vol. 2, pp. 161–173, 2013.

[10] M. C. Saha, H. Mahfuz, U. K. Chakravarty, M. Uddin, M. E. Kabir, and S. Jeelani, “Effect of density, microstructure, and strain rate on compression behavior of polymeric foams,” Materials Science and Engineering A, vol. 406, no. 1-2, pp. 328–336, oct 2005.

[11] T. R. Walter, A. W. Richards, and G. Subhash, “A Unified Phenomenological Model for Tensile and Compressive Response of Polymeric Foams,” Journal of Engineering Materials and Technology, vol. 131, no. 1, p. 011009, 2009.

[12] D. Zenkert and M. Burman, “Tension, compression and shear fatigue of a closed cell polymer foam,” Composites Science and Technology, vol. 69, no. 6, pp. 785–792, 2009.

[13] M. E. Kabir, M. C. Saha, and S. Jeelani, “Tensile and fracture behavior of polymer foams,” Materials Science and Engineering A, vol. 429, no. 1-2, pp. 225–235, 2006.

[14] M. Avalle, G. Belingardi, and A. Ibba, “Mechanical models of cellular solids: Parameters identification from experimental tests,” International Journal of Impact Engineering, vol. 34, no. 1, pp. 3–27, jan 2007.

[15] R. S. Ayyagari and M. Vural, “Multiaxial yield surface of transversely isotropic foams: Part IModeling,” Journal of the Mechanics and Physics of Solids, vol. 74, no. 2015, pp. 49–67, jan 2015.

[16] D. S. Cronin and S. Ouellet, “Low density polyethylene, expanded polystyrene and expanded polypropylene: Strain rate and size effects on mechanical properties,” Polymer Testing, vol. 53, pp. 40–50, aug 2016.

[17] R. Huang, P. Li, and T. Liu, “X-ray microtomography and finite element modelling of compressive failure mechanism in cenosphere epoxy syntactic foams,” Composite Structures, vol. 140, pp. 157–165, 2016.

[18] N. J.Mills, R. Sta¨mpfli, F.Marone, and P. A. Bru¨hwiler, “Finite element micromechanics model of impact compression of closed-cell polymer foams,” International Journal of Solids and Structures, vol. 46, no. 3-4, pp. 677–697, Feb 2009.

[19] M. Shafiq, R. S. Ayyagari, M. Ehaab, and M. Vural, “Multiaxial yield surface of transversely isotropic foams: Part II - Experimental,” Journal of the Mechanics and Physics of Solids, vol. 76, no. 2015, pp. 224–236, 2015.

[20] C. M. Ford and L. J. Gibson, “Uniaxial strength asymmetry in cellular materials: An analytical model,” International Journal of Mechanical Sciences, vol. 40, no. 6,pp. 521–531, 1998.

[21] S. Youssef, E. Maire, and R. Gaertner, “Finite element modelling of the actual structure of cellular materials determined by X-ray tomography,” Acta Materialia, vol. 53, no. 3, pp. 719–730, 2005.

[22] R. P. Chhabra, “Non-Newtonian fluids: An introduction,” Rheology of Complex Fluids, pp. 3–34, 2010.

[23] M. Avalle, G. Belingardi, and R. Montanini, “Characterization of polymeric structural foams under compressive impact loading by means of energy-absorption diagram,” International Journal of Impact Engineering, vol. 25, no. 5, pp. 455–472,2001.

[24] Y. Chen, R. Das, and M. Battley, “Effects of cell size and cell wall thickness variations on the stiffness of closed-cell foams,” International Journal of Solids and Structures, vol. 52, no. 7-8, pp. 150–164, jan 2015.

[25] A. C. Kaya, P. Zaslansky, A. Nikolaus, and C. Fleck, “Tensile failure observations in sintered steel foam struts revealed by sub-micron contrast-enhanced microtomography,” Materials and Design, vol. 105, pp. 190–200, 2016.

[26] A. Elmoutaouakkil, L. Salvo, E. Maire, and G. Peix, “2D and 3D characterization of metal foams using x-ray tomography,” Advanced Engineering Materials, vol. 4, no. 10, pp. 803–807, 2002.

[27] S. Tammas-Williams, H. Zhao, F. Le´onard, F. Derguti, I. Todd, and P. B. Prangnell, “XCT analysis of the influence of melt strategies on defect population in Ti-6Al-4V components manufactured by Selective Electron Beam Melting,” Materials Characterization, vol. 102, pp. 47–61, 2015.

[28] O. Jirousˇek, T. Doktor, D. Kyty´, P. Zla´mal, T. F´ıla, P. Koudelka, I. Jandejsek, and D. Vav´ık, “X-ray and finite element analysis of deformation response of closed cell metal foam subjected to compressive loading,” Journal of Instrumentation, vol. 8, no. 2, 2013.

[29] A. D. Brydon, S. G. Bardenhagen, E. A. Miller, and G. T. Seidler, “Simulation of the densification of real open-celled foam microstructures,” Journal of the Mechanics and Physics of Solids, vol. 53, no. 12, pp. 2638–2660, 2005.

[30] N. C. Fahlbusch, J. L. Grenestedt, andW. Becker, “Effective failure behavior of an analytical and a numerical model for closed-cell foams,” International Journal of Solids and Structures, vol. 97 98, pp. 417–430, 2016.

[31] K. Gao, J. A. van Dommelen, and M. G. Geers, “Microstructure characterization and homogenization of acoustic polyurethane foams: Measurements and simulations,” International Journal of Solids and Structures, vol. 100-101, pp. 536–546, dec 2016.

[32] B.M. Patterson, K. A. Defriend Obrey, C. E. Hamilton, and G. J. Havrilla, “Three dimensional density measurements of ultra low density materials by X-ray scatter using confocal micro X-ray fluorescence spectroscopy,” X-Ray Spectrometry, vol. 41, no. 4, pp. 253–258, 2012.

[33] a. Elmoutaouakkil, G. Fuchs, P. Bergounhon, R. Pres, and F. Peyrin, “Three dimensional quantitative analysis of polymer foams from synchrotron radiation x-ray microtomography,” Journal of Physics D: Applied Physics, vol. 36, no. 10A, pp. A37–A43, 2003.

[34] D. V. W. M. de Vries, “Characterization of polymeric foams,” Eindhoven University of Technology, no. July, p. 34, 2009.

[35] S. Zhang, J.M. Dulieu-Barton, R. K. Fruehmann, and O. T. Thomsen, “A Methodology for Obtaining Material Properties of Polymeric Foam at Elevated Temperatures,” Experimental Mechanics, vol. 52, no. 1, pp. 3–15, 2012.

[36] D. A. Williams and R. A. Lopez-Anido, “Strain rate and temperature effects of polymer foam core material,” Journal of Sandwich Structures &Materials, vol. 16, no. 1, pp. 66–87, 2014.

[37] S. Zhang, J. M. Dulieu-Barton, and O. T. Thomsen, “The effect of temperature on the failure modes of polymer foam cored sandwich structures,” Composite Structures, vol. 121, pp. 104–113, 2015.

[38] A. Chrysochoos, “Infrared thermography applied to the analysis of material behavior: A brief overview,” Quantitative InfraRed Thermography Journal, vol. 9,no. 2, pp. 193–208, 2012.

[39] Y. Ohbuchi, H. Sakamoto, and N. Nagatomo, “Thermal image analysis of plastic deformation and fracture behavior by a thermo-video measurement system,” Measurement Science and Technology, vol. 27, no. 12, 2016.

[40] The lasaR ac914 ballistic helmet — morgan composites and defence systems.[Online]. Available: http://www.morgandefencesystems.com/en-gb/advancedarmour/lasa-soldier-protection/lasa-ballistic-helmets/lasa-ac914-ballistic-helmet/

[41] Defence. [Online]. Available: https://www.d3o.com/defence/

[42] D3oR formable foams. [Online]. Available: https://www.d3o.com/wpcontent/uploads/2018/05/formable-foams.pdf

[43] D.Morin, G. Haugou, F. Lauro, B. Bennani, and B. Bourel, “Elasto-viscoplasticity behaviour of a structural adhesive under compression loadings at low, moderate and high strain rates,” Journal of Dynamic Behavior of Materials, vol. 1, no. 2, pp. 124–135, Jun 2015.

[44] A. ASTM D3575-14, “Standard test methods for flexible cellular materials made from olefin polymers,” ASTM, Tech. Rep., 2014.

[45] Flir x6901sc mwir. [Online]. Available: http://www.nbn.at/fileadmin/user upload/Vertretungen/FLIR/X6900sc/Datasheets/X6901sc 29267-201-en-US A4-1708-nbn.pdf

[46] W. Minkina and S. Dudzik, “Infrared Thermography: Errors and Uncertainties,” Wiley online library, 2009.

[47] T. W. Wysokinski, D. Chapman, G. Adams, M. Renier, P. Suortti, and W. Thomlinson, “Beamlines of the biomedical imaging and therapy facility at the Canadian light source - Part 3,” Nuclear Instruments and Methods in Physics Research, Section A: Accelerators, Spectrometers, Detectors and Associated Equipment, vol.775, pp. 1–4, 2015.

[48] Tech info technology overview. [Online]. Available: https://bmit.lightsource.ca/tech-info/technology-overview/